



HAL
open science

3D phase-field computations of microsegregation in nodular cast iron compared to experimental data and CalPhad-based Scheil-prediction

Janin Eiken, Emir Subasic, Jacques Lacaze

► To cite this version:

Janin Eiken, Emir Subasic, Jacques Lacaze. 3D phase-field computations of microsegregation in nodular cast iron compared to experimental data and CalPhad-based Scheil-prediction. *Materialia*, 2019, pp.100538. 10.1016/j.mtla.2019.100538 . hal-02382408

HAL Id: hal-02382408

<https://hal.science/hal-02382408>

Submitted on 27 Nov 2019

HAL is a multi-disciplinary open access archive for the deposit and dissemination of scientific research documents, whether they are published or not. The documents may come from teaching and research institutions in France or abroad, or from public or private research centers.

L'archive ouverte pluridisciplinaire **HAL**, est destinée au dépôt et à la diffusion de documents scientifiques de niveau recherche, publiés ou non, émanant des établissements d'enseignement et de recherche français ou étrangers, des laboratoires publics ou privés.

3D phase-field computations of microsegregation in nodular cast iron compared to experimental data and CalPhad-based Scheil-prediction

Janin Eiken^a, Emir Subasic^a, Jacques Lacaze^b

^aAccess e.V., Aachen, Germany

^bCIRIMAT, Université de Toulouse, Toulouse, France

The redistribution of solute elements during processing of a nodular cast iron alloy was simulated for the first time comprehensively over time and 3D space. Numerical predictions had so far been limited to 1D models, neglecting local morphological aspects and commonly also diffusion and growth in solid-state. Application of the standard multi-phase-field method was hindered by the inherent simplifying assumption of equal and constant molar volume, causing artificial piling-up of solute and biased kinetics during modelling of graphite growth. A recently developed volumetric multi-phase-field approach now accounts for the changing partial molar volume of the individual elements. The Calphad-based phase-field study was benchmarked to experimental cooling and nodule density data, and the predicted as-cast distributions were validated by experimental segregation analysis. The combined numerical and experimental findings were furthermore used as a basis to discuss simplifying assumptions commonly made in 1D Scheil-type models.

1. Introduction

3D computations of microsegregation contribute to a better understanding and control of microstructure evolution and as-cast material properties. The multicomponent multi-phase-field (MMPF) method [1,2] implemented in the Micress[®] software [3] offers the possibility to simulate microsegregation in a comprehensive way under consideration of finite liquid and solid diffusivities, nucleation conditions and morphological aspects. The coupling to thermodynamic databases enables handling of complex multicomponent multiphase quasi-equilibria, while diffusion matrixes can consistently be derived from mobility databases. Calphad-coupled MMPF simulations have become state of the art for steels [3,4] and many other technical alloys [5-7], however not yet for alloys that exhibit significant volume change during solidification. This is especially true for nodular cast irons where graphite forms in a divorced eutectic transformation, with graphite expanding upon crystallization while austenite is shrinking. While the volume change itself might be of minor interest for microsegregation prediction, it is indispensable to consider the intrinsic transport of matter and solute, since all elements forming part of the material are changing position as consequence of local expansion or shrinkage. Neglect of the expansion-related solute transport during simulation of nodular cast irons was found to result in unrealistic kinetics and incorrect microsegregation prediction [8]. In the present work, a novel volumetric multi-phase-field (Vol-MMPF) approach [8], which in contrast to the standard MMPF formulation [1,2] accounts for volume change and related matter and solute transport, was applied to study microsegregation in a representative nodular cast iron alloy. Phase-specific partial molar volumes were evaluated as function of temperature and composition from the linked Calphad database.

Microsegregation in cast irons is of importance as it affects the mechanical and chemical properties of cast iron not only directly, but also indirectly by its interplay with microstructure evolution. Negative segregation of graphitizers (Si, Al, Cu, Ni) and positive segregation of cementite stabilizers (Mn, Cr, Mo, V) is known to decrease the stable graphite-austenite eutectic transformation temperature and promote formation of detrimental intercellular carbides in the last stage of solidification, while local impoverishment of nodularizers (Mg, Ce) may affect the graphite morphology [9-12]. High concentration gradients of specific substitutional elements such as Ni and Si are expected to reduce the carbon diffusion flux and thus

favour detrimental chunky growth [15]. Microsegregation also controls the subsequent solid-state eutectoid transformation with some of the named elements promoting ferrite, while others promoting pearlite formation [16-19]. In the studied representative nodular cast iron alloy (Fe-3.66 C-1.97 Si-0.18 Mn-0.048 Mg), diffusion of C controls the overall evolution kinetics, Si is acting as graphitizer, Mn as carbide-stabilizer and Mg as nodularizer.

To our knowledge, this is the first time that microsegregation during processing of a multicomponent cast iron was simulated in 3D space. A previous multicomponent 2D MMPF study [20] was restricted to nucleation and growth of graphite in the early solidification stage where volume change is still negligible. The important role of volume change during graphite growth was demonstrated for a binary Fe-C alloy by 2D cellular automaton simulations [21,22], however the pragmatic way expansion was handled is not extendable to multicomponent alloys. A general problem of 2D simulations compared to 3D simulations is that diffusion lengths are systematically overestimated because the volume to radius ratio of the nodules and the surrounding shells is not correctly reproduced. To date, 1D models based on spherical coordinates are still the method of choice to predict microsegregation in cast iron alloys. The majority of existing models is based on the Scheil approach, i.e. the mass balance is solved for a closed volume under assumption of infinite diffusion in liquid and zero diffusion in solid phases [23]. Scheil-type models neglect local morphological aspects and cannot provide multidimensional distribution maps, but allow for a fast estimation of solute contents as function of solid fraction. The predictivity of Scheil-type models was in early applications [24,25] still limited by use of calibrated partition coefficients, but strongly increased with combined multicomponent thermodynamic modelling [26]. For comparison with the Vol-MMPF simulations, we generated concentrations curves with the TC-Scheil module of the ThermoCalc software [27]. The TC-approach is in contrast to some extended Scheil-type models [28,29] merely based on thermodynamic data and does not consider any process conditions. Among other aspects, we try to clarify the controversially discussed question whether change in cooling conditions or nodule density has a strong impact on microsegregation [12-16, 28-31].

The study further encompasses a casting experiment to provide realistic process conditions for input and to validate the Vol-MMPF simulations. The paper starts with a description of the experimental casting procedure and the experimental microsegregation analysis. Afterwards the novel Vol-MMPF-approach is explained, followed by the simulation scenario and the numerical microsegregation analysis. Both experimental and numerical results are then discussed together and eventually compared to Scheil predictions.

2. Experimental procedure

The samples used in this work were obtained by casting a ferritic SGI grade EN-GJS-400-18-LT in a furan resin sand mould. The total casting weight – including gating system and pouring basin – was approx. 6000 kg. The casting experiment was carried out using an induction melting furnace, an automatized magnesium-wire melt treatment, in-ladle inoculation and manually controlled melt pouring. The melt quality was controlled by Quik-Cup thermal analysis and composition measurement in the foundry laboratory using LECO analysis for carbon and sulphur and mass spectrometry for all other elements. The melt temperature was measured by use of a thermocouple lance during successive stages of melt preparation. Just before pouring, it was 1320°C and the chemical composition was slightly hypoeutectic at 3.66 C, 1.97 Si, 0.18 Mn and 0.048 Mg (in weight % with all other elements as traces). The casting geometry consisted of five blocks of different sizes which enabled studying the effect of varying cooling rates. All blocks but the smallest one (50 x 50 x 150 mm) were cube-shaped with edges of 150, 300, 500, and 750 mm. The temperature profiles were recorded during solidification and subsequent cooling to room temperature by 13 type N thermocouples. Four samples - named M4, M8, M10, and M13 - were taken from defined positions, such that the metallography analysis could clearly be related to the recorded temperatures profiles T4, T8, T10, and T13 depicted in figure 1.

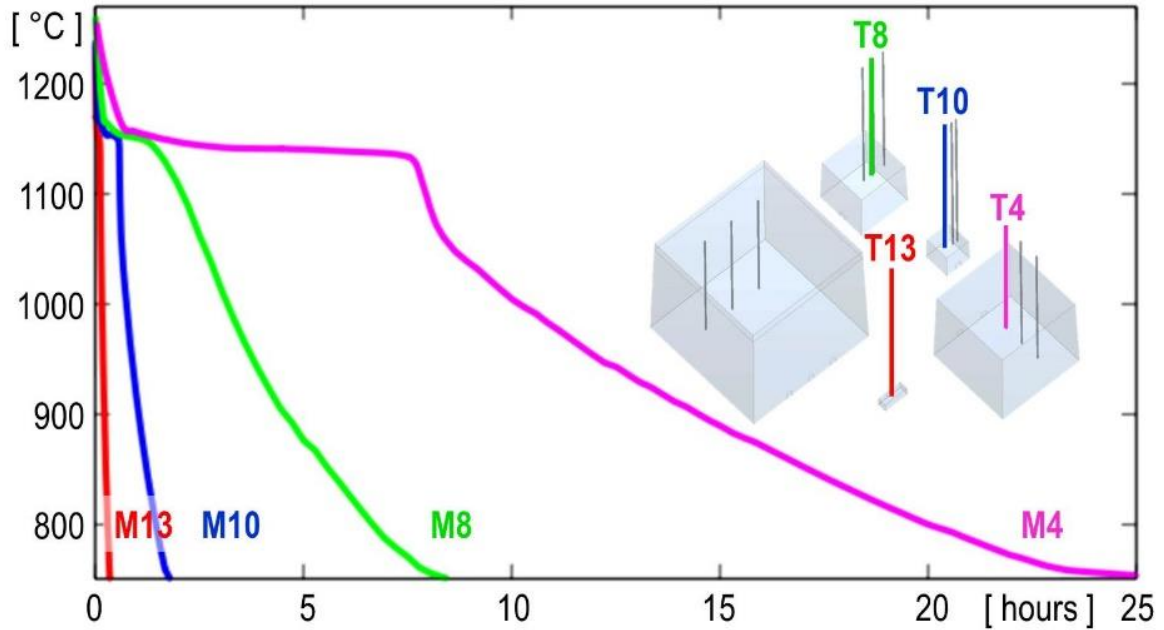


Figure 1: Measured cooling curves for samples M4, M8, M10 and M13.

From each of the four samples, five micrographs were prepared to characterize the graphite nodule size and spatial density. The nodule density N_A , the nodule diameters D_A , and the overall fraction of graphite f_G were evaluated using an automatic image analysis software. To avoid bias by micropores or inclusions, only graphite nodules with a diameter above a certain threshold were taken into account [32]. Area fraction and volume fraction of graphite were assumed to be equal. 3D nodule densities N_V and mean diameters \bar{d}_V were derived in two different ways: a) based on the simplifying assumption of randomly distributed mono-sized spheres and b) based on Saltykov's method of inverse diameters [33]:

$$N_V = \frac{N_A}{\bar{d}_V} \quad \text{with a) } \bar{d}_V = \frac{4}{\pi} \bar{d}_A \quad \text{or} \quad \text{b) } \bar{d}_V = \frac{\pi}{2} (\overline{d_A^{-1}})^{-1}. \quad (1)$$

Table 1 gives both the directly measured as well as the derived data for the different samples. As expected, the nodule diameter decreases with increasing cooling rate while the nodule density is increasing. No clear tendency could be found for the impact of the cooling rate on graphite fraction.

Table 1: Experimental characterization of graphite nodule size and spatial density

sample	fraction		mean nodule diameter [mm]			nodule density [mm ⁻²], [mm ⁻³]		
	f_G	\bar{d}_A	\bar{d}_V (a)	\bar{d}_V (b)	N_A	N_V (a)	N_V (b)	
M04	0.10	0.062	0.079	0.083	35	443	424	
M08	0.11	0.043	0.055	0.058	69	1260	1171	
M10	0.08	0.028	0.036	0.041	116	3254	2824	
M13	0.10	0.023	0.029	0.030	225	7683	7553	

3. Experimental microsegregation analysis

Two samples, M10 and M13, were selected for experimental microsegregation analysis. For analysing the distribution of substitutional solutes Si and Mn, energy dispersive X-ray analyses (EDX) were carried out with a XFLASH 6130 from Bruker fitted in a FEI Quanta scanning electron microscope (SEM). The procedure was two-fold: First, acquiring 2D maps for visualization of the microsegregation features (see figure 2); Second, recording spectra by spot counting on a regular grid for quantitative analysis. During these analyses, Fe, Si, and Mn were measured together with Al that was sometimes detected, but associated to the final polishing of the samples and thus disregarded. Amongst the raw data, a significant number of data points show a sum much lower than 100%. These points were related to graphite particles and removed from further analysis of the solute distribution in the matrix. The selected data were corrected for atomic number, fluorescence and absorption, and the sum of Fe, Si, and Mn was normalized to 100%. Grid analyses were performed with a grid spacing of 175 μm in both directions, large enough to ensure a representative statistics independent of the different spacing of dendrite arms, nodules and eutectic cells. The corrected concentrations values were then sorted in decreasing order for Si and in increasing order for Mn accounting for their opposite segregation behaviour. The resulting 1D-distribution profiles (figure 3) provide a statistical characterization of the element distribution in the entire multidimensional structure. This is in contrast to some previous studies e.g. [12,31], where only limited areas between selected adjacent nodules were analysed and extreme values distributed at a scale much larger than the nodule spacing may not have been considered. It should however be noted that the evaluation of the extreme concentrations generally exhibits a very high uncertainty due to the intrinsic scattering of X-ray emission [34] as well as due to the statistical randomness to directly hit the singular points of last solidification. To avoid bias by the finite size and number of the measuring points, we restricted the range of the cumulative distribution from 0 to 99%.

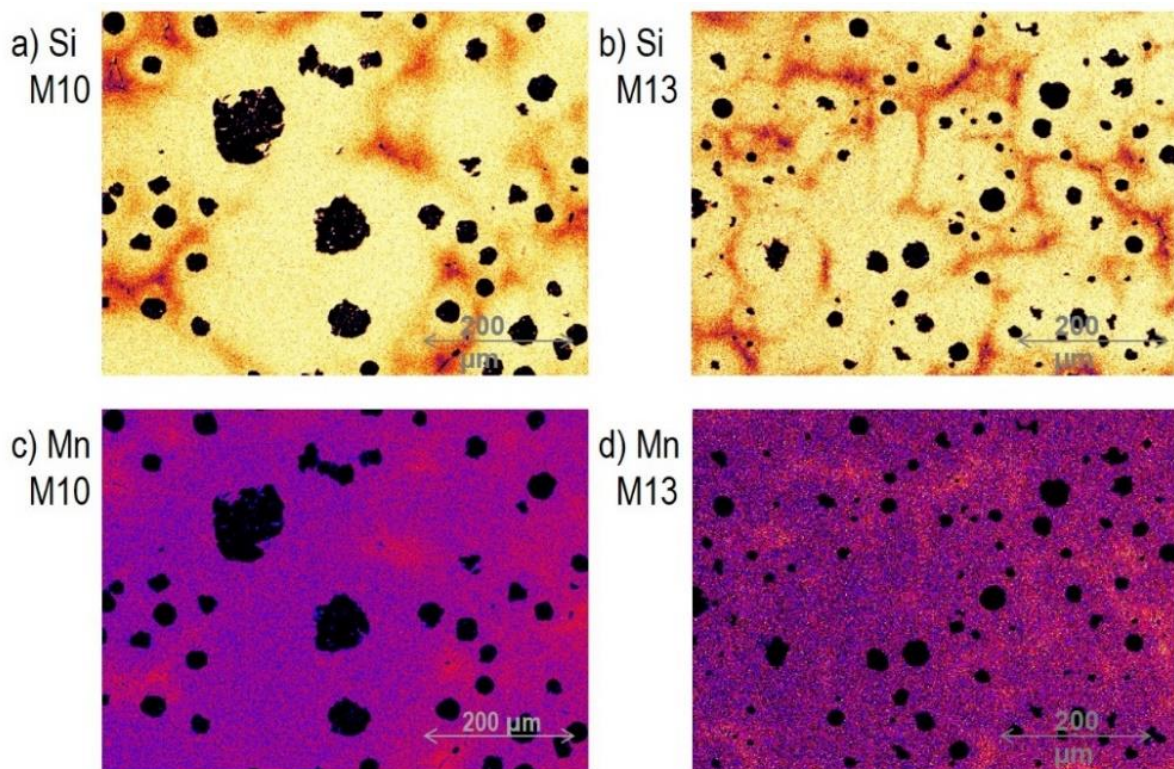


Figure 2: Measured distributions maps of silicon and manganese for samples M10 and M13

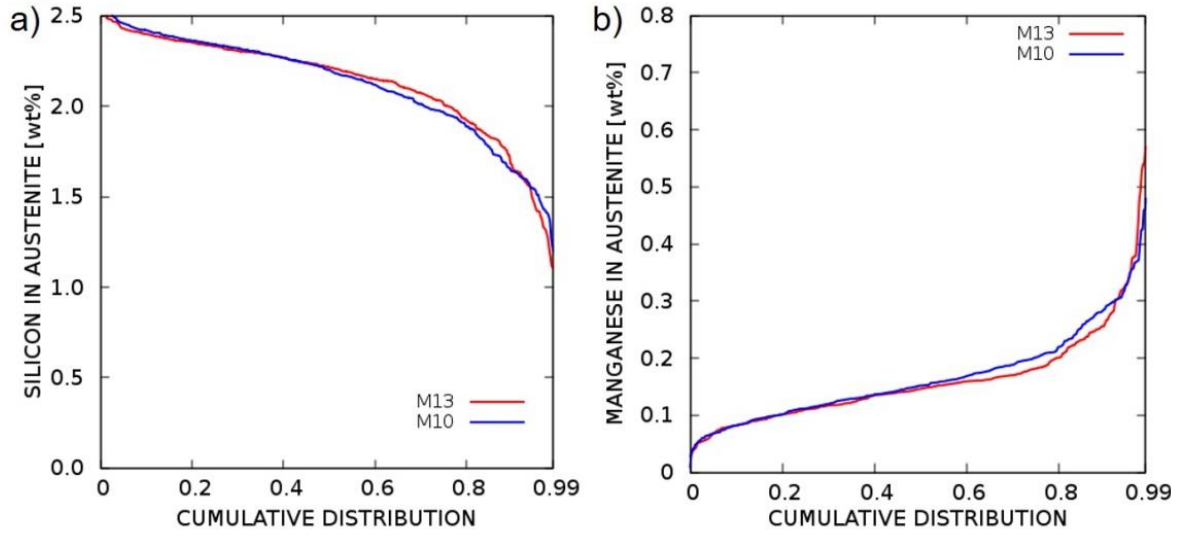


Figure 3: Experimental segregation curves for silicon and manganese in samples M10 and M13.

4. The volumetric multicomponent multi-phase-field model (Vol-MMPF)

Microstructure simulations were performed with the Micress[®] software [1,2,3] based on a novel Vol-MMPF approach [8] which accounts for volume changes during phase transformation and cooling. Thermodynamic data were derived from the database TCFE8 [35] and diffusivities from the mobility database mobFe3 [36] via the TQ-interface of the Thermo-Calc software [27]. In the following, the material-specific modelling of nucleation, anisotropic growth, solute segregation and volumetric expansion are shortly described.

4.1 Modelling of austenite and graphite nucleation

Nucleation is handled in Micress[®] by a submodel. Nuclei, whose radii can be much smaller than the grid spacing Δx , are generated when the local undercooling - evaluated from the thermodynamic database - exceeds the specified critical undercooling. In order not to violate the concentration balance, the initial nucleus composition still equals that of the surrounding melt, but local equilibrium is soon obtained by solute redistribution. As long as a nucleus is too small to be numerically resolved, its curvature is analytically evaluated from the volume fraction under assumption of spherical geometry [2]. Austenite was modelled to nucleate with low nucleation undercooling ($\Delta T_{\text{crit}} = 1^\circ\text{C}$) in one of the domain corners and with higher undercooling ($\Delta T_{\text{crit}} = 10^\circ\text{C}$) on the liquid/graphite interface. Nucleation of graphite was modelled on seeds randomly distributed in the melt according to a size-density function with almost exponential course (figure 4). The seeds were distributed to eleven classes with radii ranging from 0 to 1 μm and the corresponding critical undercooling for nucleation ΔT_{crit} was evaluated according to Turnbull's free growth criterion [37] by:

$$\Delta T_{\text{crit}} = \frac{2\sigma_{\text{LG}}^0}{\Delta s_{\text{LG}} r_{\text{seed}}}. \quad (2)$$

where σ_{LG}^0 denotes the mean interfacial energy and Δs_{LG} the local entropy of fusion evaluated from the database. Since the critical undercooling is inversely proportional to the seed radius r_{seed} , nucleation starts at the largest seeds. Under slow cooling conditions only a low undercooling is reached and smaller seeds do not become active, hence less graphite nodules are nucleated than for higher cooling

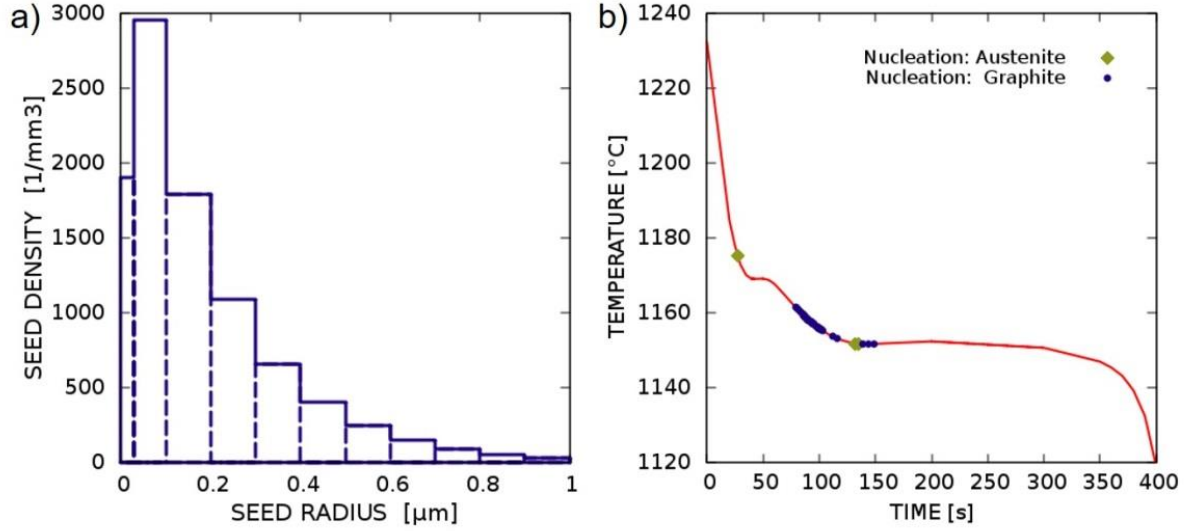


Figure 4: a) Calibrated seed distribution for graphite nucleation, b) nucleation events in sample M13.

rates. The total seed density was adjusted to approximately reproduce the experimental nodule densities given in Table 1. Note that the intention was not at all to obtain a perfect fitting, but rather to study whether, and if so, how changing nodule densities affect microsegregation.

4.2 Modelling of austenite and graphite growth

A set of multiple phase-fields $\phi_\alpha(\mathbf{x}, t)$ maps the spatial distribution of the phases liquid (L), austenite (A) and graphite (G) in the simulation domain. Additionally, grains of same phase, but different orientation, may be distinguished. The evolution of the structure is described by a set of multiphase-field equations:

$$\dot{\phi}_\alpha(\mathbf{x}, t) = \sum_\beta M_{\alpha\beta}^\phi \left(|\nabla\phi_{\alpha\beta}| v_{\text{mol},\alpha\beta}^{-1} \Delta\mu_{\alpha\beta} - \sigma_{\alpha\beta} K_{\alpha\beta} + \sum_\gamma J_{\alpha\beta\gamma} \right), \quad (3)$$

where the phase field variable ϕ_α is associated with the local mole fraction of phase α , interacting with multiple phases β . $\Delta\mu_{\alpha\beta}$ denotes the difference in chemical potential and $v_{\text{mol},\alpha\beta}$ the mean molar volume for interacting grains α and β . Their ratio represents the thermodynamic driving force for transition and is evaluated via the TQ-interface of the Thermo-Calc software as function of local composition and temperature. The pairwise interface contributions $\sigma_{\alpha\beta} K_{\alpha\beta}$ correspond to the capillarity force. Third-order interface contributions $J_{\alpha\beta\gamma}$ account for forces only acting in junctions where more than two grains are locally coexisting, for details see [1,2]. $\sigma_{\alpha\beta}$ denotes the interfacial energy and $M_{\alpha\beta}$ the interfacial mobility, specifically defined for each pairwise phase interaction as function of the interfacial normal vector \mathbf{n} . The anisotropy description of the liquid-austenite interface accounts for the cubic symmetry of the fcc-lattice:

$$M_{LA} = M_{LA}^0 a_{\text{cubic}}(\mathbf{n}), \quad (4)$$

$$\sigma_{LA} = \sigma_{LA}^0 a_{\text{cubic}}(\mathbf{n}), \quad (5)$$

$$a_{\text{cubic}}(\mathbf{n}) = 1 - \delta_{LA} 4(n_x^4 + n_y^4 + n_z^4 - 0.75), \quad (6)$$

where the mean interface mobility M_{LA}^0 was defined in the diffusion controlled limit [39] and the mean liquid/austenite interface energy was set to $\sigma_{LA}^0 = 0.17 \text{ Jm}^{-2}$ with an anisotropy of $\delta_{LA} = 0.05$.

Graphite nodules are supposed to be multi-crystalline, built of multiple conical sectors as sketched in figure 5a. The effective interface of a spheroid is hence formed of basal c-facets modelled in the Micress software by:

$$M_{LG} = M_{LG}^0 a_{\text{facet}}(\theta), \quad (7)$$

$$\sigma_{LG}^* = \sigma_{LG}^0 a_{\text{facet}}^{-1}(\theta), \quad (8)$$

$$a_{\text{facet}}(\theta) = \delta_{LG} + (1 - \delta_{LG}) |\tan \theta| \tanh(|\tan \theta|^{-1}), \quad (9)$$

with phase-specific values $M_{LG}^0 = 5 \cdot 10^{-15} \text{ m}^4 \text{ J}^{-1} \text{ s}^{-1}$, $\delta_{LG} = 0.5$ and $\sigma_{LG}^0 = 1.5 \text{ Jm}^{-2}$ [38]. θ denotes the angle between the local interfacial normal vector and the nearest facet vector and σ_{LG}^* is the regularized interfacial stiffness. Figure 5b shows the effective Wulff shape of a graphite spheroid modelled with 50 facets. The graphite/austenite interface was modelled based on the same anisotropy function with specific values $M_{GA}^0 = 8 \cdot 10^{-16} \text{ m}^4 \text{ J}^{-1} \text{ s}^{-1}$ and $\sigma_{GA}^0 = 1.2 \text{ Jm}^{-2}$. Note that the interface anisotropy is of marginal importance for the studied microsegregation and only described for the sake of completeness. All interfacial mobility values were corrected in the thin-interface limit by:

$$M_{\alpha\beta}^\phi = \frac{M_{\alpha\beta}}{1 + \eta \cdot G \cdot M_{\alpha\beta}}, \quad (10)$$

where the factor G is locally evaluated from the database to consider the growth restricting effect of the diffusion-controlling elements in the multiphase interface region [39]. The numerical interfacial thickness was set to $\eta = 3.5 \Delta x$ with Δx being the numerical grid size. High accuracy was ensured by a special finite-difference formulation with implicit correction of systematic discretization errors [40].

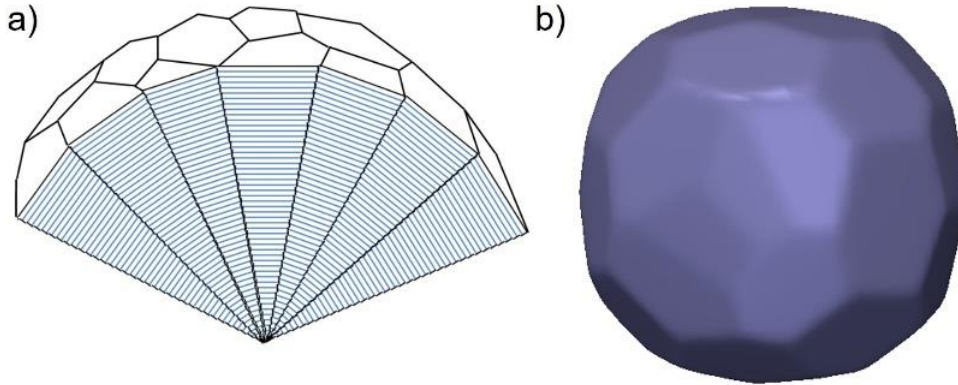


Figure 5: Schematic cut through a graphite nodule (a) and Wulff-shape of the effective anisotropy function.

4.3 Modelling of solute segregation and diffusion

The composition vector field $\vec{\chi}(\mathbf{x}, t)$ maps the distribution of the alloying elements during simulation. The components of this vector give the content of the solute elements C, Si, Mn, and Mg in terms of mole fractions, with n_{mol}^i denoting the number density of moles of this component and n_{mol} the total number density of moles (eq. 11). Within the diffuse interface region where the adjacent phases overlap, the vector $\vec{\chi}$ is defined as a mixture composition consisting in the weighted sum of individual phase-specific composition vectors $\vec{\chi}_\alpha$, evaluated from the phase-related mole number densities $n_{\text{mol},\alpha}^i$ and $n_{\text{mol},\alpha}$:

$$\bar{\chi}(\mathbf{x},t) = \sum_{\alpha} \phi_{\alpha}(\mathbf{x},t) \bar{\chi}_{\alpha}(\mathbf{x},t), \quad \text{with } \chi^i = \frac{n_{\text{mol}}^i}{n_{\text{mol}}} \quad \text{and} \quad \chi_{\alpha}^i = \frac{n_{\text{mol},\alpha}^i}{n_{\text{mol},\alpha}}. \quad (11)$$

Redistribution of the mixture composition $\bar{\chi}$ into individual phase-specific composition $\bar{\chi}_{\alpha}$ is done according to the quasi-equilibrium approach which postulates equal diffusion potentials $\tilde{\mu}_{\alpha}^i = \tilde{\mu}_{\beta}^i$ for each component in locally coexisting phases. This constraint corresponds to a parallel tangent construction and is evaluated by coupling to the database TCFE8 with intermediate extrapolation [1,2]. Solute diffusion of the elements C, Si, Mn, Mg (including cross dependencies) is simulated in both liquid and austenite:

$$\dot{\bar{\chi}}(\mathbf{x},t) = n_{\text{mol}}^{-1}(\mathbf{x},t) \left(\sum_{\alpha} \nabla \cdot [n_{\text{mol}}(\bar{\mathbf{x}},t) \bar{\mathbf{j}}_{\alpha}(\mathbf{x},t)] + \nabla \cdot [n_{\text{mol}}(\bar{\mathbf{x}},t) \bar{\mathbf{j}}_{\text{atc}}(\mathbf{x},t)] \right), \quad (12)$$

$$\text{with diffusion fluxes } \bar{\mathbf{j}}_{\alpha}(\mathbf{x},t) = \bar{\bar{D}}_{\alpha} \nabla \bar{\chi}_{\alpha}(\mathbf{x},t). \quad (13)$$

Equation (12) represents a generalized formulation of the diffusion equation, allowing for locally changing mole number densities $n_{\text{mol}}(\bar{\mathbf{x}},t)$. The phase-specific diffusion matrices $\bar{\bar{D}}_{\alpha}$ are evaluated as product of thermodynamic factor and chemical mobility from the databases TCFE8 [35] and mobFe3 [36]. In between the frequent database calls, the diffusion coefficients are interpolated based on Arrhenius-type functions. By default, antitrapping currents $\bar{\mathbf{j}}_{\text{atc}}$ [39] were evaluated by the Micress[®] software, but found to be negligible except for the first seconds of dendritic growth. It is important to note that equation (12) ensures conservation of the total number of moles of each species over the simulation domain, while the constraint of conserved mole fractions used in the standard multi-phase-field model [1,2] is not valid in the general case of unequal mole number density. The local number density of moles $n_{\text{mol}}(\mathbf{x},t)$ remains unaffected by substitutional diffusion, but changes during interstitial diffusion of C at the rate of:

$$\dot{n}_{\text{mol}}(\mathbf{x},t) = \nabla \cdot [n_{\text{mol}}(\mathbf{x},t) \mathbf{j}_A^C(\mathbf{x},t)], \quad (14)$$

where \mathbf{j}_A^C is the diffusion flux of C in austenite as defined in eq.(13). The explicit computation of the composition vector accounts for both the change in mole fraction (eq.12) and the change in total mole number density (eq. 14):

$$\bar{\chi}(\mathbf{x},t+\Delta t) = [\bar{\chi}(\mathbf{x},t) + \dot{\bar{\chi}}(\mathbf{x},t) \Delta t] \frac{n_{\text{mol}}(\mathbf{x},t)}{n_{\text{mol}}(\mathbf{x},t) + \dot{n}_{\text{mol}}(\mathbf{x},t) \Delta t}. \quad (15)$$

4.4 Modelling of volume change

The eutectic transformation in nodular cast-iron is controlled by carbon transport through the austenite shell. As long as the carbon atoms are interstitially dissolved in austenite they hardly contribute to the material's volume, but drastically increase their partial volume when becoming attached to the graphite interface. Effectively, the graphite nodules grow by volume expansion, pushing the surrounding austenite shell to the outside. If we were to neglect the displacement of the fcc-lattice and the related solute transport in the simulation, we would find all slow diffusing elements piling up in front of the graphite interface. This would falsify the segregation profiles and lead to transition kinetics orders of magnitude lower than in reality as demonstrated on the example of a ternary Fe-C-Si alloy [8]. Note that expansion-induced matter transport is not limited to solidification, but also occurs by creep processes in solid-state. A comprehensive modelling of solid and fluid mechanics during microstructure evolution of a multicomponent alloy would clearly exceed the possibilities of today's computation, especially as the mechanical processes occur on a time-scale much faster than diffusion. Because of the elevated temperatures during processing, it is reasonable to assume that any temporary stress is immediately relaxed. The new

Vol-MMPF approach allows a realistic prediction of phase volumes, transformation kinetics and multi-component microsegregation based on the assumption that local strain gradients in liquid or solid phases are immediately homogenized by internal matter fluxes.

The model accounts for the fact that the local molar volume may change as a consequence of phase transition, solute diffusion or cooling. The phase-specific molar volumes \bar{v}_α are evaluated from the database as function of composition and temperature. Within the diffuse interfacial regions, we define the local molar volume v_{mol} as the weighted sum of the individual phase-specific molar volumes v_α :

$$v_{\text{mol}}(\mathbf{x}, t) = \sum_\alpha [\phi_\alpha(\mathbf{x}, t) v_\alpha(\bar{\chi}_\alpha, T)]. \quad (16)$$

To homogenize the local volume changes and continuously recover a stress-free simulation domain, internal molar fluxes \mathbf{j}_{mol} are calculated based on a relaxation approach on a time scale much faster than diffusion and growth ($\Delta\tau \ll \Delta t$).

$$\mathbf{j}_{\text{mol}}(\mathbf{x}, \tau) = v_{\text{mol}}^{-1}(\mathbf{x}) M_V \nabla [n_{\text{mol}}(\mathbf{x}, \tau) v_{\text{mol}}(\mathbf{x})], \quad (17)$$

$$n_{\text{mol}}(\mathbf{x}, \tau + \Delta\tau) = n_{\text{mol}}(\mathbf{x}, \tau) + \nabla \cdot \mathbf{j}_{\text{mol}}(\mathbf{x}, \tau), \quad (18)$$

Note that the term $(n_{\text{mol}} v_{\text{mol}})$ is a measure for local strain. The matter fluxes \mathbf{j}_{mol} become zero, when no more gradients in local strain exist. As the relaxation is assumed to be instantaneous, the relaxation coefficient M_V can be defined as a numerical parameter adjusted for computational efficiency and the local molar volume v_{mol} is modelled as temporary constant. The relaxation equation is solved iteratively at the end of each phase-field time step Δt until a homogeneously distributed volume is recovered, i.e. until the mean gradient $\nabla(n_{\text{mol}} v_{\text{mol}})$ has fallen below a numerically negligible limit, here specified as 10^{-5} % of the mean value of $n_{\text{mol}} v_{\text{mol}}$. Simultaneously to eq. (18), the local composition vector field is recalculated in each iteration step $\Delta\tau$ to account for the expansion-related solute fluxes:

$$\bar{\chi}(\mathbf{x}, \tau + \Delta\tau) = n_{\text{mol}}^{-1}(\mathbf{x}, \tau + \Delta\tau) (\bar{\chi}(\mathbf{x}, \tau) n_{\text{mol}}(\mathbf{x}, \tau) + \nabla [\bar{\chi}(\mathbf{x}, \tau) \mathbf{j}_{\text{mol}}(\mathbf{x}, \tau)]) \quad (19)$$

5. Phase-field simulations

Phase-field simulations were performed for the various process conditions referring to the casting samples M4, M8, M10 and M13 described in section 2. The nominal composition indicated in section 2 was used ($w^C = 3.66$, $w^{\text{Si}} = 1.97$, $w^{\text{Mn}} = 0.18$ and $w^{\text{Mg}} = 0.048$ in weight-%). Simulations start at the moment when all cavities were filled with melt. The temperature evolution was imposed to follow the measured cooling curves T4, T8, T10, and T13 depicted in figure 1 from $T \approx 1230^\circ\text{C}$ down to $T \approx 752^\circ\text{C}$, i.e. to the onset of the eutectoid transformation. The initial volume of the cubic calculation domain was $(200 \mu\text{m})^3$ and the numerical grid spacing $\Delta x = 2 \mu\text{m}$. To check the influence of the numerical discretization, sample M13 which exhibited the finest structure - and hence was most critical - was additionally run with a smaller grid spacing of $\Delta x = 1 \mu\text{m}$. This comparative simulation confirmed that the changed resolution had no visible effect on the resulting segregation profiles.

All simulations started from pure liquid phase. As the alloy was slightly hypoeutectic, primary austenite nucleated prior to graphite at about 1175°C and then grew dendritically. Below 1161.5°C graphite nodules started to nucleate and grow from the melt with spherical morphology. After becoming encapsulated either by primary austenite or by newly nucleated eutectic austenite, the nodules continued to grow driven by carbon diffusion through the austenite shell. Some new graphite nodules nucleated during further cooling. Table 2 gives a characterization of the simulated graphite distribution, namely the graphite fraction, the mean diameter of the nodules at the end of the simulation, the nodule number

within the calculation volume and the corresponding nodule density. The highest number of nodules was obtained in sample M13. Figure 4b shows the time and temperature of nucleation events for this sample and figure 6 illustrates the microstructure evolution during the various stages of nucleation and growth. Solidification was here completed at about $T_S \approx 1117^\circ\text{C}$, while in the slowest solidifying sample M4, solidification ended at $T_S \approx 1140^\circ\text{C}$. The final stage of the simulation was governed by solid-state transformation with graphite directly growing from austenite. All simulations were stopped at 752°C , i.e. the eutectoid transformation was not modelled.

Table 2: Characterization of simulated volume fraction, size, number and number density.

sample	volume fraction	mean diameter D_V	nodule number	density N_V [mm^{-3}]
M04	0.100	0.088	2	250
M08	0.100	0.046	12	1500
M10	0.099	0.039	20	2500
M13	0.097	0.028	60	7500

Volume change was considered during all simulations. As expected, primary growth of austenite resulted in local contraction, while growth of graphite caused local expansion and hence reduced the overall shrinkage. The total volume of the hypoeutectic alloy continuously decreased dominated by thermal shrinkage. The effective volume change resulting from the balance of expansion, contraction, and thermal shrinkage was about -5% from pouring until start of eutectoid transformation. Note that in the present simulations, the total number of moles has been kept constant and neither liquid feeding nor pore formation was considered.

A general problem of studying the impact of cooling time and nodule density on microsegregation based on experimental data is that both parameters do not vary independently in practice. Slower cooling implicitly results in reduced nucleation undercooling and hence in a reduced nodule density. On the other hand, a change in nucleation density will alter the latent heat release and thus the eutectic undercooling. In contrast to experiments, Vol-MMPF-simulations enable an independent variation of both parameters by explicit adjustment of the seed density function. To study the separate effect of cooling and nodule density, two variations of the experimental process conditions were simulated: Variation1 (V1) combines the nodule count from sample M13 with the cooling from sample M10 and Variation2 (V2) combines the cooling from sample M13 with the nodule count from sample M10.

6. Numerical microsegregation analysis

As direct simulation results, 3D distribution maps of the solute elements were given out at specified time steps. Figure 7 shows the 3D distribution of the substitutional elements Si and Mn evaluated for samples M10 and M13 at the end of simulation. Note that all compositions were converted to weight fraction. To enable a quantitative comparison with both experimental results and Scheil prediction, the 3D maps were further processed into characteristic 1D profiles. Concentrations belonging to the austenite region were filtered by the constraint that the local phase-field value of austenite exceeds the critical value of $\phi_\alpha = 0.5$. In accordance with the processing of the experimental data described in section 3, the concentration of the solute elements were sorted independently from each other - accounting for their segregation behaviour- and plotted versus the normalized cumulative distribution of value numbers. Figure 8 shows the segregation profiles of Si and Mn, and figure 9 the profiles of Mg and carbon for samples M4, M8, M10 and M13. All curves refer to a temperature of 752°C . Carbon distributions are additionally shown for $T = 1117^\circ\text{C}$. Furthermore, selected 2D sections of the Si distribution at different times during solidification are given in figure 10, and figure 11 shows a 2D section of the final carbon concentration field for simulations M13, V1, V2 and M10 in comparison. All numerical results are discussed in the following section together with the experimental data.

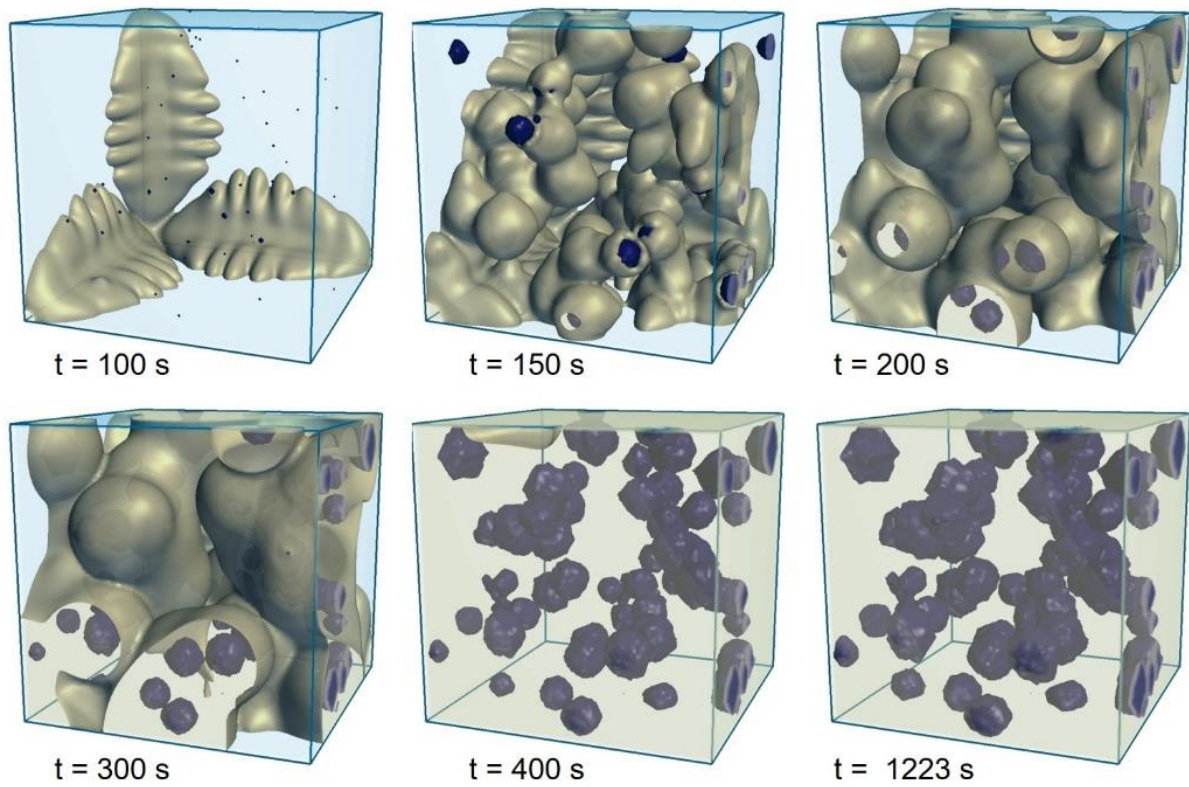


Figure 6: Phase-field simulation of the microstructure evolution in sample M13 during cooling from $T = 1230^{\circ}\text{C}$ to $T = 752^{\circ}\text{C}$.

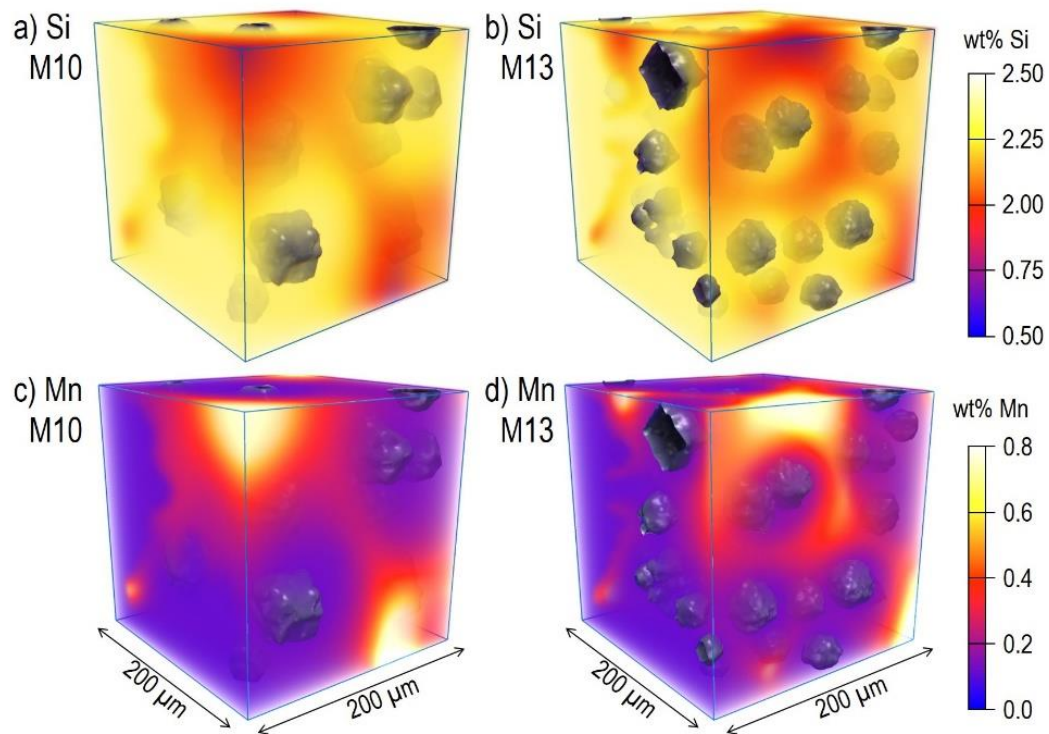


Figure 7: Simulated distributions of silicon and manganese for samples M10 and M13 at $T = 752^{\circ}\text{C}$.

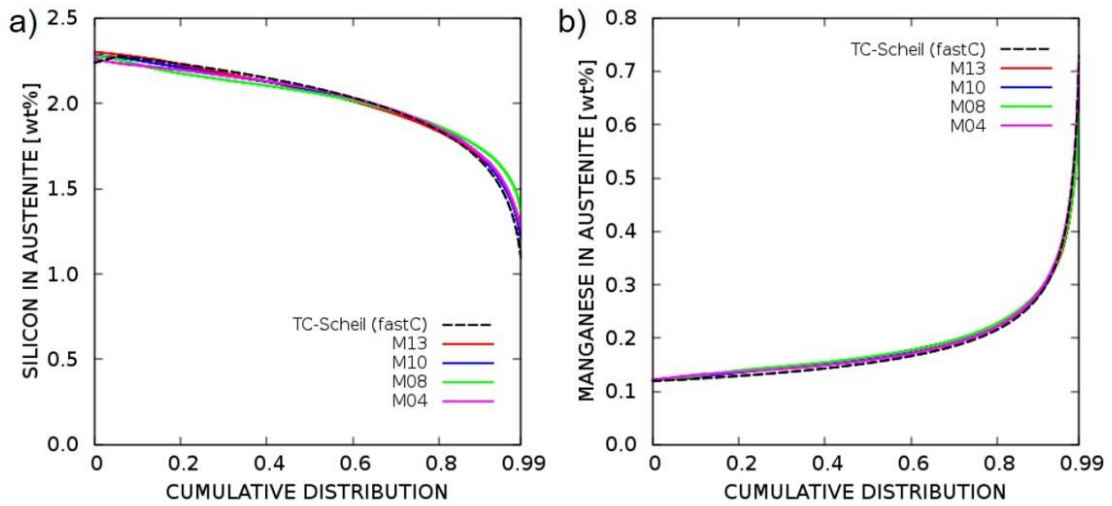


Figure 8: Simulated segregation curves of silicon and manganese for samples M4, M8, M10 and M13 at $T = 752^{\circ}\text{C}$ in comparison with TC-Scheil calculations.

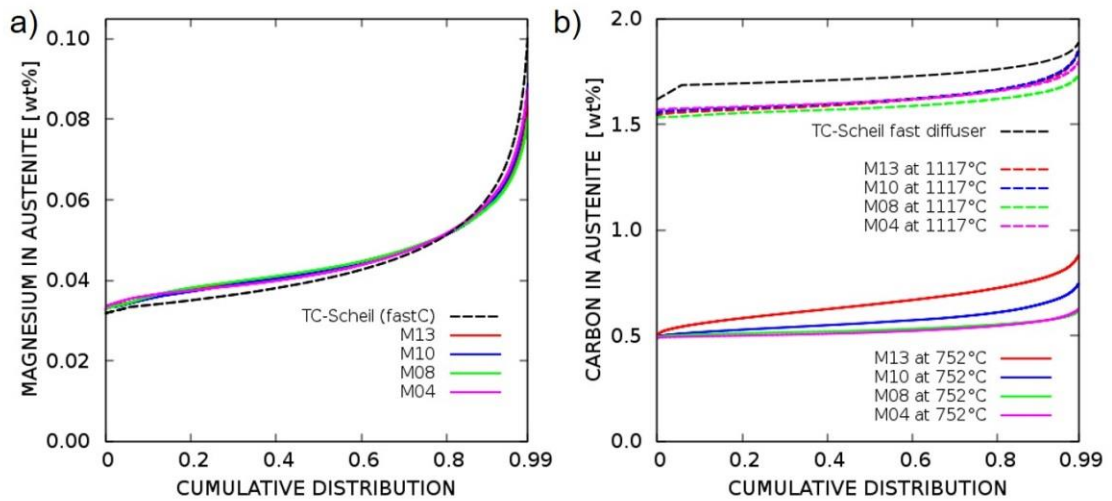


Figure 9: Simulated segregation curves of magnesium and carbon for samples M4, M8, M10 and M13 at $T = 752^{\circ}\text{C}$ (and additionally at $T = 1117^{\circ}\text{C}$ for carbon).

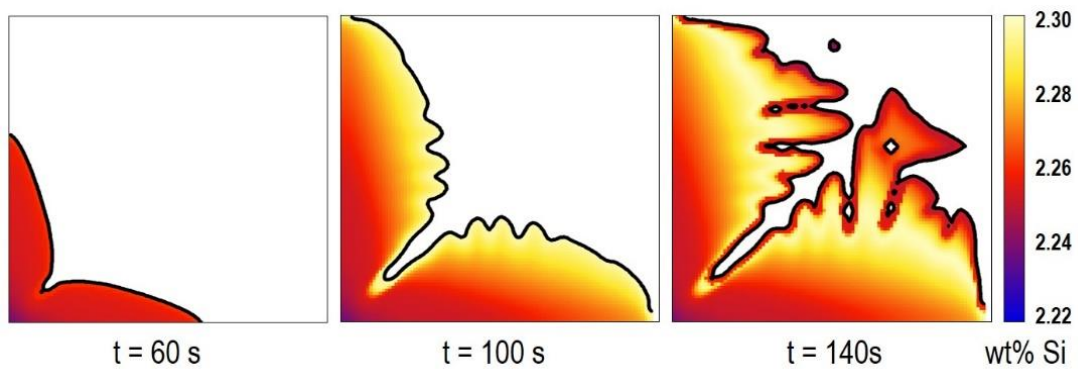


Figure 10: 2-D section cut from PF-simulation. The silicon content in austenite increases during proeutectic solidification, but decreases during eutectic growth.

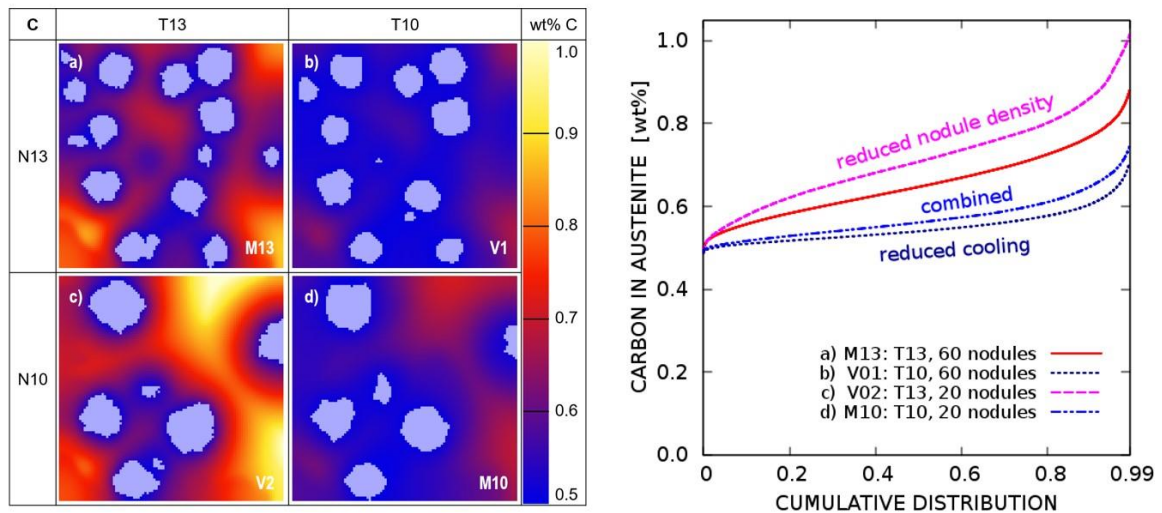


Figure 11: Carbon distribution from independent variation of process parameters a) sample M13, b) variant V1 with reduced cooling, c) variant V2 with decreased nodule count, d) sample M10 with reduced cooling and decreased nodule count combined.

7. Combined discussion of experimental and numerical results

4.5 Microsegregation of substitutional elements

For a first qualitative validation, the numerically predicted 3D distribution maps of Si and Mn depicted in figure 7 were compared to the experimentally evaluated 2D maps in figure 2. Both show similar segregation patterns with lowest Si contents and highest Mn contents in the regions of last solidification. An important result of the multidimensional analysis is that the extreme values corresponding to the end of solidification are unevenly spread along the intercellular boundaries at a scale which can be much larger than the nodule spacing. The observed impoverishment of the graphitizing element in the residual melt combined with the simultaneous enrichment of the cementite stabilizer principally promotes cementite and carbide formation in the last stages of solidification, which was however found to be uncritical under the given conditions. Only very small amounts of cementite were detected in some samples with fraction below 0.5%. An interesting detail observed in the 3D simulations is that the Si content of austenite still increases during primary pro-eutectic growth, despite the fact the partition coefficient of Si is greater than one (figure 10). This atypical segregation behaviour was reported before [28] and can be explained by the strong composition and temperature dependency of the partition coefficient. After nucleation of graphite, the Si content of austenite starts to decrease. Consequently, highest values in the multidimensional Si distribution map mark the moment of first eutectic precipitation as illustrated by the 2D sections in figure 10. The 3D distribution maps of Mg (not depicted here) were found to be qualitatively comparable to those of Mn, showing lowest values in the dendrite's centre and highest values in the last solidified regions. Mg segregation and associated precipitation of Mg-compounds are known to have a significant impact on the graphite morphology. Whether this affect is dominated by modification of kinetics, interfacial energies or nucleation and to which extent the interplay with oxygen and sulphur plays a role is still unclear and shall be the subject of a future study.

A quantitative validation of the numerical simulation results was enabled by processing the multi-dimensional data into characteristic 1D profiles. In contrast to simple line-scans, these profiles are not subjectively biased and ensure a statistical representation of the whole microsegregation spectrum distributed over different length scales. Experimentally and numerically evaluated profiles (figure 3 vs figure 8) of both Si and Mn show good agreement except for deviation within the first 20% of the distribution which are most probably related to the physical noise generally associated with EDX measurements [34]. The

experimental validation confirms that the new Vol-MMPF approach produces realistic results without the need for parameter fitting. The only parameter which was calibrated is the nodule density which however obviously has no significant effect on the characteristic 1D profiles of the substitutional elements.

Indeed, the most striking result of the microsegregation analysis is that the characteristic profiles of none of the substitutional elements (figures 3, 8, 9a) exhibit any significant difference for the samples M4, M8, M10 and M13 processed under significantly differing cooling conditions. These results go against the still widely accepted theory that microsegregation in cast iron strongly depends on cooling rate [12,13,30,31], but finds support in the difficulty of ascertaining this statement in practical studies [14,26,28,29]. The present study goes beyond the previous studies, demonstrating that variation of the process times ranging from 20 min to 25 h and related change in nodule density from approx. $0.4 \cdot 10^{12}$ to $7.6 \cdot 10^{12} \text{ m}^{-3}$ show no significant impact on the characteristic 1D segregation curves. Independent variation of cooling condition and nodule density in simulations V1 and V2 revealed a slightly enhanced, however still negligible impact. It is however important to note that this statement only holds for the characteristic 1D concentration profiles, which do not account for spatial aspects. While the statistical distribution remain unaffected, the multidimensional distribution patterns considerably alter with changing process consideration. The 3D distribution maps (figure 7) generally reveal increased spatial concentration gradients for higher nodule densities, because the concentration variation occurs over reduced segregation lengths. In contrast to classic 1D models, the new Vol-MMPF model can provide these more comprehensive local information.

4.6 Microsegregation of carbon

In addition to the microsegregation of the substitutional elements, also the redistribution of carbon was predicted by the Vol-MMPF model. As carbon is interstitially dissolved in austenite, its diffusion coefficient is still relative high at 1175°C ($3.7 \cdot 10^{-10} \text{ m}^2\text{s}^{-1}$), but decreases during cooling to 752°C by two orders of magnitude. During the eutectic transformation, carbon continuously diffuses from the liquid/austenite interface to the graphite/austenite interface. Nevertheless, the residual melt becomes more and more enriched in carbon and the highest carbon concentrations in austenite are obtained at the point of last solidification. Figure 9 shows that the carbon concentration profiles of all four samples are still close to each other at the end of solidification. During subsequent cooling to eutectoid temperature all curves are significantly shifted downward because of the continuous decrease of carbon concentration at the graphite-austenite interface and resulting diffusion fluxes towards the graphite nodules. At the final temperature of 752°C , the maximum carbon values reveal a clear impact of the process conditions, while the minimum value is identical for all samples. The highest carbon concentration is obtained in the fastest solidifying sample M13, clearly followed by M10. However, the profiles of M08 and M04 hardly differ, which can be explained by the fact that the impact of increased cooling time and decreased nodule density compensate each other, i.e. increasing diffusion time is compensated by longer diffusion distances.

The 2D sections depicted in figure 11 give further insight into the fundamental segregation mechanisms. Figure 11a correspond to simulation M13. Minimal carbon concentrations are located at the graphite/austenite interface and maximal concentrations in places with largest distance to a graphite nodule. Figure 11b shows the same section for simulation V1 where reduced cooling was assumed. The increased diffusion time here results in a homogenization of the profile and thus a decrease of the maximal values. The minimal values - determined by the local equilibrium condition at the interface - do not change. A reduced nodule density, in contrast, results in longer diffusion distances and thus in higher maximum concentrations as shown in figure 11c. Combination of both variations in sample M10 (figure 11d) results in partial compensation. In this specific case, the effect of the cooling change was found to slightly dominate, which however cannot be generalized and may depend on the specific casting conditions.

8. Comparison to Scheil predictions

Scheil computations were performed with the Thermo-Calc Scheil module [21] based on the same thermodynamic database as used for the Vol-MMPF simulations. The TC-model accounts for multicomponent interdependencies with carbon defined as fast-diffuser, i.e. with infinite diffusivity. Figures 8-10 show that the TC Scheil predictions are - for all solute elements but carbon - almost identical to the simulated distribution curves and hence also in good agreement with the experimental data. This result is by far not trivial taking into account the different ways these curves were obtained. The statistic 1D curves were generated from post-mortem data, i.e. by sorting the concentration data of the final 3D structure in progressive order. Scheil concentrations, in contrast, are local equilibrium values continuously evaluated during solidification and originally function of fraction solid, but here correlated to the cumulative distribution, i.e. a dimensionless rank number which indicates the relative positioning of a specific concentration within the spectrum of all occurring concentrations. A correlation between cumulative distribution and solid fraction is only reasonable provided that all concentrations are unambiguously ascending or descending with time. This holds for Mn and Mg, but not strictly for Si, which exhibits an atypical temporarily increase during pro-eutectic growth as discussed in section 7.1. A changing curve progression generally requires a different sorting of the simulation data e.g. with respect to a leading element or a weighted rank number [7]. As consequence of the simplified sorting, we observe a small, however almost negligible, deviation from Scheil in the very first part of the simulated distribution curve in figure 8.

Furthermore, cumulative distributions can only be related to fraction solid values provided that local concentrations at the solid/liquid interface are simply frozen in during solidification and not further affected by back-diffusion. This seems to be a reasonable assumption for all substitutional elements, as the substitutional diffusion coefficients in austenite evaluated from the mobility database were found to be more than four orders lower compared to the diffusion coefficient of interstitial carbon, which controls the eutectic transition. Nevertheless, back-diffusion plays an important role during the very last stage of solidification. Here, the exponentially evolving concentration gradients cause non-negligible concentration fluxes which eventually determine the end of solidification. Due to the inherent neglect of back-diffusion, Scheil predictions can theoretically never reach 100% solid and the concentrations asymptotically approach infinity or zero. In the present study, Scheil computations were stopped at 99% fraction solid.

In contrast to Scheil computations, Vol-MMPF simulations comprehensively address the solid-state process. A critical question was whether the concentration profiles built up in austenite during solidification would become partially homogenized by diffusion during the subsequent cooling to 752°C. This was expected to be most likely for sample M4, exposed to the longest cooling time (25 h), but found not to be the case for any of the substitutional elements. Only carbon is strongly affected by finite solid-phase diffusion and can therefore not be predicted by the Scheil model. It is noteworthy that despite the assumption of infinite diffusivity in the Scheil model, the carbon content does not homogenize in austenite due to the multicomponent interdependency of its diffusion potential with the slow diffusing elements.

Good matching between statistical post-mortem data and Scheil predictions furthermore requires that the microsegregation is not affected by the continuing growth of the graphite nodules after solidification. Since graphite forms completely from carbon, all other elements have to be transported out of the evolving interfacial regions. This transport is however induced by volume expansion and hence, the substitutional elements move together with the displaced Fe-lattice, thus only changing their local position, but not their characteristic profiles. In fact, the statistical 1D profiles of Si, Mn and Mg evaluated at the end of simulation (752°C) showed no visible deviation from those evaluated at the end of solidification (1117°C). Moreover, these profiles were found in good agreement with the experimental profiles evaluated at room temperature, i.e. after the eutectoid transformation has taken place. This finding supports the hypothesis that the eutectoid structure inherits the substitutional solute content of the as-solidified

austenitic structure [19]. It is emphasized that this only holds for substitutional elements, but not for carbon, whose concentrations profile strongly changes during solid state transition and completely deviates from Scheil prediction (figure 9).

Most revealing is to recall that the TC-Scheil computations are merely based on thermodynamic data and - in contrast to the Vol-MMPF simulations - do not consider any process conditions. Nevertheless, statistical concentration profiles evaluated from simulations with strongly varying cooling and nucleation conditions reveal no significant deviation from Scheil predictions. This supports the finding that the concentration statistics of substitutional elements are independent of any process specific conditions. Non-negligible deviation from Scheil prediction may only be expected when extremely long process times are combined with very high nodule densities.

Altogether, it can be summarized that the statistical concentration distribution of substitutional elements in ductile cast iron can reliably be predicted by the TC-Scheil model provided that matter is conserved. The benefits of this prediction are however limited by the fact that neither corresponding carbon concentrations nor information about the spatial distribution of the solute elements is provided. In comparison, the new Vol-MMPF model is computationally more expensive, but provides comprehensive 3D distribution maps for all solutes as function of time, essential to study local effects e.g. on graphite degeneration or carbide formation.

9. Conclusions

Microsegregation in hypoeutectic ductile cast iron was studied for the first time in 3D space based on a novel volumetric multicomponent multi-phase-field (Vol-MMPF) approach. The Calphad-based simulations were successfully validated for a representative Fe-C-Si-Mg-Mn alloy by a simultaneous experimental study. The combined numerical and experimental microsegregation analysis confirms the assumption that the statistical distribution of substitutional elements in the final microstructure is simply inherited from the as-solidified structure and not significantly affected by on-going graphite growth or diffusion in solid-state. Against the common view that microsegregation is strongly affected by process conditions, only the characteristic profiles of interstitial carbon revealed a sensitivity to varying cooling and nucleation conditions, while characteristic 1D profiles of substitutional elements hardly differed from each other or from TC-Scheil predictions. In contrast to the merely statistical 1D profiles, the complex 3D distribution patterns and local chemical gradients, however, considerably alter with varying nodule density. The new Vol-MMPF model can provide this more comprehensive information and contribute to a better understanding and control of the interplay between microsegregation and structure evolution in cast iron alloys.

Acknowledgement

The authors like to thank Alexandre Freulon for sample preparation, Yannick Thébaud for performing EDX measurements, and the German Federal Ministry for Economic Affairs and Energy for partial funding of the work in the frame of the research project DiWaGussGJS.

References

- [1] J. Eiken, B. Böttger, I. Steinbach, Multiphase-field approach for multicomponent alloys with extrapolation scheme for numerical application, *Phys. Rev. E* 73 (2006) 066122.
- [2] J. Eiken, *A Phase-Field Model for Technical Alloy Solidification*, Shaker Verlag (2010) ISBN 978-3-8322-9010-8.
- [3] MICRESS® multicomponent multi-phase-field software, www.micress.de, pre-release version 6.350.

- [4] B. Böttger, M. Apel, J. Eiken, P. Schaffnit, I. Steinbach, Phase-Field Simulation of Solidification and Solid-State Transformations in Multicomponent Steels, *Steel Res. Int.*, 79:8 (2008) 608-616
- [5] Y. Shen, S. Yang, J. Liu, H. Liu, R. Zhang, H. Xu, Y. He., Study on Micro Segregation of High Alloy Fe–Mn–C–Al Steel. *Steel Res. Int.* (2019) 1800546
- [6] J. Eiken, M. Apel, S.M. Liang, R. Schmid-Fetzer, Impact of P and Sr on solidification sequence and morphology of hypoeutectic Al–Si alloys: Combined thermodynamic computation and phase-field simulation. *Acta Materialia* 98 (2015) 152-163.
- [7] K. Grätz, J. Eiken, R. Schmid-Fetzer, Methods of segregation analysis applied to simulated multi-component multiphase microstructures, *Int. J. Mater. Res.* 105:2 (2014) 130-138.
- [8] J. Eiken, B. Böttger, A Multi-phase-field Approach for Solidification with Non-negligible Volumetric Expansion - Application to Graphite Growth in Nodular Cast Iron, *T. Indian I. Metals* (2018) 71(11), 2725-2729.
- [9] P.C.Liu, C.R. Loper, Segregation of Certain Elements in Cast Irons, *AFS Trans.* 92 (1984) 289–295.
- [10] A. Kagawa, T. Okamoto, Partition of alloying elements on eutectic solidification of cast iron, *MRS Proc.* 34 (1984) 201.
- [11] N.K. Datta, N.N. Engel, Electron Microprobe Study of the Distribution of Si, Cu, Ni, Mn, Mo, and Cr in Ductile iron, *AFS Trans.* 83 (1976) 431-436.
- [12] A. Owhadi, J. Hedjazi, P. Davami, M. Fazli, J.M. Shabestari, Microsegregation of manganese and silicon in high manganese ductile iron. *Mater Sci Tech-lond* 13(10), (1997) 813-817.
- [13] S. Pietrowski, G. Gumienny, Microsegregation in Nodular Cast Iron with Carbides, *Archives of Foundry Engineering* 12:4 (2012) 127-134
- [14] Charbonnier J, Margerie JC. Contribution to the study of microsegregation in Fe-C casting alloys, *Mem. Sci. Rev. Met.* 64 (1967) 345-357.
- [15] B. Pustal, B., A. Bührig-Polaczek, Physico-chemical causes of the formation of chunky graphite in austenitic ductile iron. *Acta Mater* 124 (2017) 137-142.
- [16] M.J. Lalich, C.R. Loper, Effects of pearlite promoting elements on the kinetics of the eutectoid transformation in ductile cast irons, *AFS Trans.* 81 (1973) 217-228.
- [17] E.N. Pan, M.S. Lou, C.R. Loper, Effects of Cu, Sn, and Mn on the eutectoid transformation of graphitic cast irons, *AFS Trans.* 95 (1987) 819–840.
- [18] J. Lacaze, The austenite to Pearlite/ferrite transformation, *ASM Handbook 1A* (2017) 106-113.
- [19] A. Freulon A, P. de Parseval P, C. Josse, J. Bourdie, J. Lacaze, Study of the Eutectoid Transformation in Nodular Cast Irons in Relation to Solidification Microsegregation, *Metall. Mater. Trans. A* 74 (2016) 5362-5371.
- [20] A. Sommerfeld, B. Böttger, B. Tonn, Graphite nucleation in cast iron melts based on solidification experiments and microstructure simulation, *J. Mater. Sci. Technol.* 24 3 (2008) 321-324
- [21] M. Zhu, L. Zhang, L., H. Zhao, D.M. Stefanescu, Modeling of microstructural evolution during divorced eutectic solidification of spheroidal graphite irons, *Acta Mater* (2015) 84, 413-425.
- [22] A.A. Burbelko, D. Gurgul, M. Królikowski, M. Wróbel, Cellular automaton modeling of ductile iron density changes at the solidification time, *Arch. Foundry Eng.* 13(4), (2013) 9-14.
- [23] E. Scheil, Bemerkungen zur Schichtkristallbildung, *Zeitschrift für Metallkunde* 34 (1942) 70-72.
- [24] R. Boeri, F. Weinberg, Microsegregation in Ductile Iron, *AFS Trans.* 97 (1989) 179-184.
- [25] R. Boeri, F. Weinberg, Microsegregation of Alloying Elements in Cast Iron, *Cast Metals* 6:3 (1993) 153-158.
- [26] B. Domeij, A. Diószegi, Inferring the development of microsegregation and microstructure in Spheroidal and Compacted Graphite Iron using EPMA-WDS, *Proc. of the 6th Int. Conf. on Solidification Processing SP17* (2017) 455-458.
- [27] Thermo-Calc software. www.thermocalc.com.
- [28] J. Lacaze, Solidification of spheroidal graphite cast irons, Part III: microsegregation related effects, *Acta mater.* 47:14 (1999) 3779-3792.
- [29] C. Selig, J. Lacaze, Study of microsegregation buildup during solidification of spheroidal graphite cast iron, *Metall. Mater. Trans.* 31B (2000) 827-836.

- [30] L. Nastac, D. M. Stefanescu, Modeling of Microsegregation in SG Cast Iron. AFS Trans 101, (1993) 933-938.
- [31] A. Tadesse, H. Fredriksson, H, On the solidification and structure formation during casting of large inserts in ferritic nodular cast iron, Metall. Mater. Trans. B 49(3), (2018) 1223-1235.
- [32] A. Escobar, D. Celentano, M. Cruchaga, J. Lacaze, B. Schulz, P. Dardati, A. Parada, Experimental and numerical analysis of effect of cooling rate on thermal-microstructural response of spheroidal graphite cast iron solidification, Int. J. Cast. Met. Res. 27:3 (2014) 176-186.
- [33] S.A. Saltykow, Stereometrische Metallographie, VEB Dt. Verlag für Grundstoffindustrie, 1974.
- [34] J. Lacaze, P. Benigni, A. Howe, Some Issues Concerning Experiments and Models for Alloy Microsegregation, Adv. Eng. Mater. 5 (2003) 37-46.
- [35] TCFe8, TCS Steels/Fe-Alloys Database, version 8.0.
- [36] TCS Steels/Fe-Alloys Mobility Database, version 3.0.
- [37] D. Turnbull, Theory of catalysis of nucleation by surface patches, Acta Metall. 1 (1953) 8-14.
- [38] R.H. McSwain, C.E. Bates, W.D. Scott, Iron-graphite surface phenomena and their effects on iron solidification, AFS Trans. 82 (1974) 85-94.
- [39] A. Carré, B. Böttger, M. Apel, Implementation of an antitrapping current for a multicomponent multiphase-field approach J. Cryst. Growth 380 (2013) 5-13.
- [40] J. Eiken, Numerical solution of the phase-field equation with minimized discretization error, IOP Conf. Ser: Mater. Sci. Eng. 33 (2012) 012105.